In situ stress state from walkaround VSP anisotropy in the Kumano basin southeast of the Kii Peninsula, Japan

AUTHOR(S):

Tsuji, Takeshi; Hino, Ryota; Sanada, Yoshinori; Yamamoto, Kiyohiko; Park, Jin-Oh; No, Tetsuo; Araki, Eiichiro; ... Roland Von Huene; Moore, Gregory; Kinoshita, Masataka

CITATION:

Tsuji, Takeshi ...[et al]. In situ stress state from walkaround VSP anisotropy in the Kumano basin southeast of the Kii Peninsula, Japan. GEOCHEMISTRY GEOPHYSICS GEOSYSTEMS 2011, 12: Q0AD19.

ISSUE DATE:

2011-09-22

URL:

http://hdl.handle.net/2433/163422

Geochemistry Geophysics Geosystems G3

Article
Volume 12, Number 9
22 September 2011
Q0AD19, doi:10.1029/2011GC003583
ISSN: 1525-2027

Published by AGU and the Geochemical Society

In situ stress state from walkaround VSP anisotropy in the Kumano basin southeast of the Kii Peninsula, Japan

Takeshi Tsuji
Graduate School of Engineering, Kyoto University, Kyoto 615-8540, Japan

Japan Agency for Marine-Earth Science and Technology, Yokosuka 237-0061, Japan (tsuji@earth.kumst.kyoto-u.ac.jp)

Ryota Hino
Research Center for Prediction of Earthquakes and Volcanic Eruptions, Tohoku University, Sendai 980-8578, Japan

Yoshinori Sanada
Japan Agency for Marine-Earth Science and Technology, Yokosuka 237-0061, Japan

Kiyohiko Yamamoto
Research Center for Prediction of Earthquakes and Volcanic Eruptions, Tohoku University, Sendai 980-8578, Japan

Retired

Jin-Oh Park
Atmosphere and Ocean Research Institute, University of Tokyo, Kashiwa 277-8564, Japan

Tetsuo No and Eiichiro Araki
Japan Agency for Marine-Earth Science and Technology, Yokosuka 237-0061, Japan

Nathan Bangs
Institute for Geophysics, University of Texas at Austin, Austin, Texas 78758, USA

Roland von Huene
Geology Department, University of California, Davis, California 95616, USA

Gregory Moore
Department of Geology and Geophysics, University of Hawai'i at Mānoa, Honolulu, Hawaii 96822, USA

Masataka Kinoshita
Japan Agency for Marine-Earth Science and Technology, Yokosuka 237-0061, Japan

[1] To reveal the stress state within the Kumano basin, which overlies the Nankai accretionary prism, we estimated seismic anisotropy from walkaround vertical seismic profiling (VSP) data recorded at Site C0009 during Integrated Ocean Drilling Program (IODP) Expedition 319. We obtained the following anisotropic parameters: (1) *P* wave velocity anisotropy derived from azimuthal normal moveout (NMO) velocity analysis, (2) *P* wave amplitude variation with azimuth, and (3) axes of symmetry of *S* wave splitting. Azimuthal variations of *P* wave velocity by ellipsoidal fitting analysis showed that *P* wave velocity anisotropy within sediments of the Kumano basin was ~5%. Both the directions of fast *P* wave velocity and strong amplitude

are aligned with the convergence vector of the Philippine Sea plate. Furthermore, *S* wave splitting analysis indicated that *S* wave polarization axes were parallel to and normal to the direction of plate subduction. These results indicate that the maximum horizontal stress at Site C0009 in the Kumano basin is in the direction of plate subduction. The horizontal differential stress estimated from the *P* wave velocity anisotropy (2.7~5.5 MPa) indicates that the maximum horizontal stress is similar in magnitude to (or a little higher than) the vertical stress.

Components: 6900 words, 12 figures.

Keywords: Nankai Trough; in situ stress; seismic anisotropy; seismogenic fault; walkaround VSP.

Index Terms: 0915 Exploration Geophysics: Downhole methods; 7240 Seismology: Subduction zones (1207, 1219, 1240); 8168 Tectonophysics: Stresses: general.

Received 25 February 2011; **Revised** 8 August 2011; **Accepted** 8 August 2011; **Published** 22 September 2011.

Tsuji, T., et al. (2011), In situ stress state from walkaround VSP anisotropy in the Kumano basin southeast of the Kii Peninsula, Japan, *Geochem. Geophys. Geosyst.*, *12*, Q0AD19, doi:10.1029/2011GC003583.

Theme: Mechanics, deformation, and hydrologic processes at subduction complexes, with emphasis on the NanTroSEIZE drilling transect
Guest Editors: D. Saffer, H. Tobin, P. Henry, and F. Chester

1. Introduction

[2] The Nankai Trough marks the convergent plate margin where the Philippine Sea plate is subducting beneath southwestern Japan (Figure 1). This subduction zone has repeatedly generated great earthquakes in excess of Mw 8 [*Ando*, 1975]. Because great earthquakes at convergent plate margins are believed to occur both at the plate interface and on mega-splay faults, there have been many seismic surveys [e.g., *Moore et al.*, 1990; *Park et al.*, 2002; *Bangs et al.*, 2004; *Moore et al.*, 2009] and intensive drilling operations [e.g., *Kinoshita et al.*, 2008] to investigate these seismogenic faults.

[3] A recent Integrated Ocean Drilling Program (IODP) drilling campaign used borehole breakouts and core sample observations to show that the stress state (principal horizontal stress orientation) changes across the seismogenic mega-splay fault [e.g., *Lin et al.*, 2010]. Maximum horizontal stress is perpendicular to the trench seaward of the mega-splay fault and parallel to it landward of the mega-splay fault, and changes again further landward to become nearly parallel to plate convergence [*Lin et al.*, 2010]. These variations in stress orientations are hypothetically explained by static stress variations during the earthquake cycle [*Wang and Hu*, 2006]. The anelastic strain recovery (ASR) measurements [*Byrne et al.*, 2009] and borehole wall failure analysis [*Chang et al.*, 2010] further revealed stress regime within the Nankai accretionary prism. Therefore, revealing the stress orientation and its magnitude should provide useful information for evaluating and monitoring seismogenic faults [e.g., *Crampin et al.*, 2008]. For this study, we used walkaround VSP data recorded at Site C0009 during IODP Expedition 319 in 2009 [*Saffer et al.*, 2009] (Figure 2a) to estimate seismic anisotropy and to reveal the stress state in Kumano basin sediments above the seismogenic mega-splay fault. This is a first attempt to reveal anisotropic properties from the walkaround VSP data acquired in the Nankai Trough region.

[4] Seismic anisotropy is a phenomenon that can be used to reveal in situ stress state [e.g., *Crampin et al.*, 2008]. Seismic anisotropy within sediments is related to the amount of fracturing (or crack) and the dominant orientation of those fractures [*Kaneshima et al.*, 1988; *Haacke and Westbrook*, 2006; *Haacke et al.*, 2009]. For rocks containing vertically aligned cracks (horizontal transverse isotropy; HTI), the fast velocity direction coincides with the direction of crack alignment; the degree of velocity difference provides information about crack density [*Crampin*, 1985]. Although horizontal layered sediment (e.g., Kumano basin sediment) generally have a vertical transverse isotropy (VTI) from bedding and compaction with a slow vertical axis [*Mavko et al.*, 1998], HTI induced by the

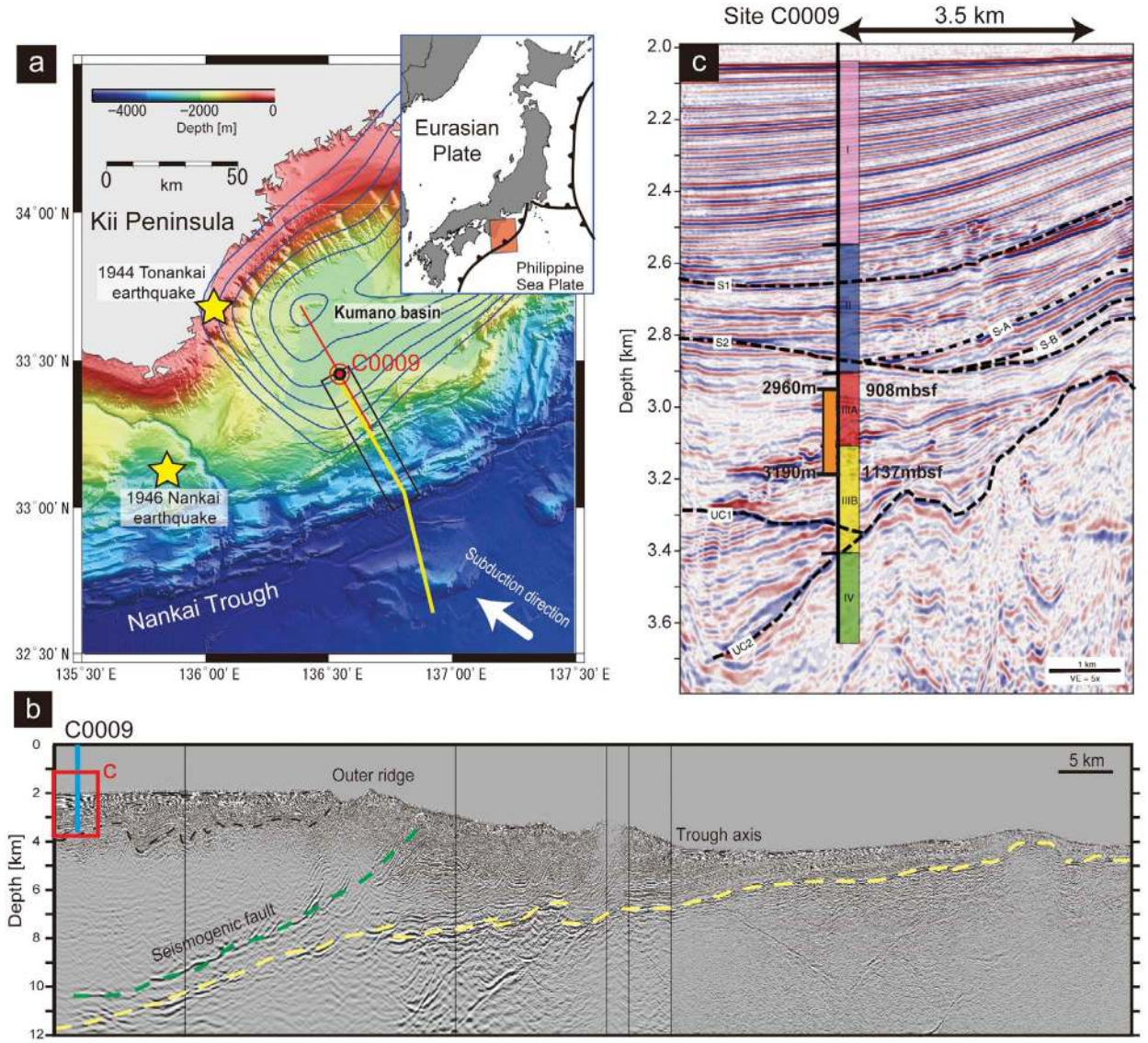

Figure 1. (a) Bathymetric map of the Nankai Trough around Site C0009. Red circle and line indicate the shooting tracks. Yellow line indicates the location of seismic profile displayed in Figure 1b. Black rectangle indicates the survey area of 3D seismic reflection data. Yellow stars mark the estimated hypocenters of the 1944 Tonankai earthquake (M 7.9) and the 1946 Nankai earthquake (M8.0). Blue contours around the Kumano basin show the coseismic slip distribution of the 1944 Tonankai earthquake [*Kikuchi et al.*, 2003]. (b) Seismic profile across Site C0009. Yellow, green, and black dashed lines indicate oceanic crust surface, mega-splay fault, and base of the Kumano basin sequence, respectively. Red rectangle indicates the location of seismic profile displayed in Figure 1c. (c) Enlarged seismic profile across Site C0009. Lithologic units defined by the *Expedition 319 Scientists* [2010] are also shown. Orange bar shows the interval where the VSI was deployed.

vertically aligned cracks are superimposed on the VTI anisotropy.

[5] If cracks are produced by a regional tectonic stress field, seismic anisotropy can be used to estimate the stress orientation and magnitude. In unconsolidated sequences, furthermore, stress-induced anisotropy due to increasing contact between grains can be observed [*Johnson et al.*, 1998]. In this case (anisotropy induced by increasing grain-contact), the fast velocity direction corresponds to the direction of principal horizontal stress. Therefore, we can evaluate stress state from azimuthal seismic anisotropy even in unconsolidated sequence [*Tsuji et al.*, 2011]. Although fractures formed during earlier deformation, under stress states possibly different from the present-day one, may also influence the seismic

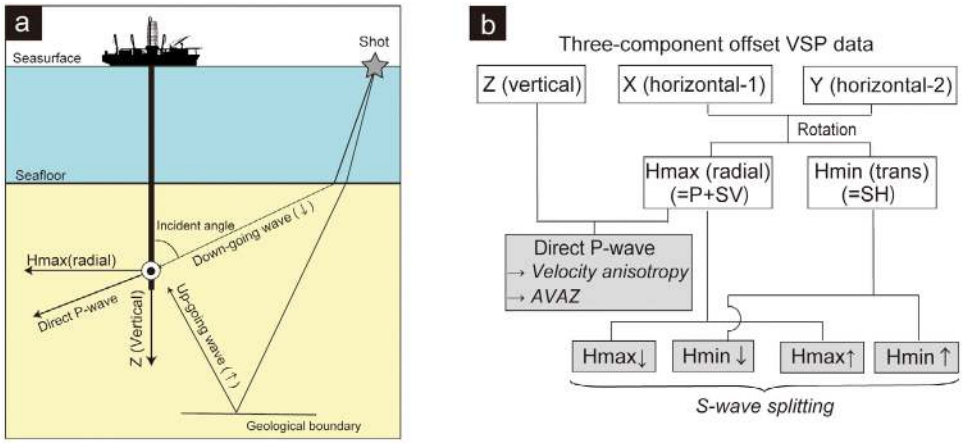

Figure 2. (a) Schematic image of the layout of the walkaround VSP survey. (b) Flow diagram illustrating wavefield separation. Gray boxes indicate the wavefields used for anisotropic analysis. From the direct *P* wave, we estimated *P* wave velocity anisotropy and amplitude variation with azimuth (AVAZ). From the horizontal components (Hmax and Hmin), we derived shear wave splitting.

anisotropy, the shallow sedimentary sequence (Kumano basin sequence) we focus on in this study was not intensively fractured, and therefore the estimated seismic anisotropy should reflect in situ stress state.

2. Geologic Setting

[6] At the Kumano transect across the Nankai Trough, the Philippine Sea Plate is subducting beneath the Japanese Islands at a convergence rate of 4.5–5.5 cm/year along an azimuth of 305–310 (Figure 1) [*Seno et al.*, 1993; *Loveless and Meade*, 2010]. Seismic reflection data (Figure 1b) show a strong negative-polarity reflection representing the mega-splay fault [e.g., *Park et al.*, 2002; *Moore et al.*, 2009]. Seismic and tsunami inversions [*Kikuchi et al.*, 2003; *Tanioka and Satake*, 2001] suggest that rupture on this mega-splay fault might have generated the 1944 Tonankai earthquake (M 7.9) and tsunami.

[7] Landward of the seafloor trace of the mega-splay fault (the outer ridge), about 1 km of Kumano basin sediments directly overlies the accretionary prism (Figure 1b). Site C0009 was located within the Kumano basin where there is ~1350 m of unconsolidated sediment overlying the accretionary prism (Figure 1c). Trough-parallel normal faults are well developed within the Kumano basin immediately landward of the outer ridge [*Park et al.*, 2002]. These normal faults may be related to dynamic activity on the mega-splay fault, tectonic evolution of the splay-fault and fore-arc basin [*Gulick et al.*, 2010], or underplating [*Leggett et al.*, 1985]. However, they are not found around Site C0009 and the stress state cannot be determined from seismic reflection profiles alone.

3. VSP Data

[8] During IODP Expedition 319, we acquired walkaway, walkaround, and zero-offset VSP data [*Saffer et al.*, 2009]. Here we use the walkaround VSP data to study azimuthal seismic anisotropy. For the walkaround VSP data, four air gun strings (128 L total volume) were deployed on R/V *Kairei* and 278 shots were recorded (Figure 3a). The shooting interval was 30 s and the distance from the borehole was almost constant at 3473–3567 m (Figure 3b).

[9] We deployed a Schlumberger's Vertical Seismic Imager (VSI) wireline tool inside 13–3/8 inch (~40 cm) casing. The receiver configuration consisted of a 16-level, three-component receiver array spaced at 15.24 m (50 feet) intervals over a depth range from 908 to 1137 m below seafloor (2960–3190 m below the sea surface; Figures 1c and 4) within the lower part of the Kumano basin sedimentary sequence. The sampling interval was 2 ms, and the record length for each shot was 20 s. Figure 5 shows the first arrivals of the VSP data (radial component) at 45° intervals of shooting position. Because the data acquired by channel 10 was noisy in the 25–30 Hz frequency band, we needed to reduce the noise for anisotropic analysis. To achieve

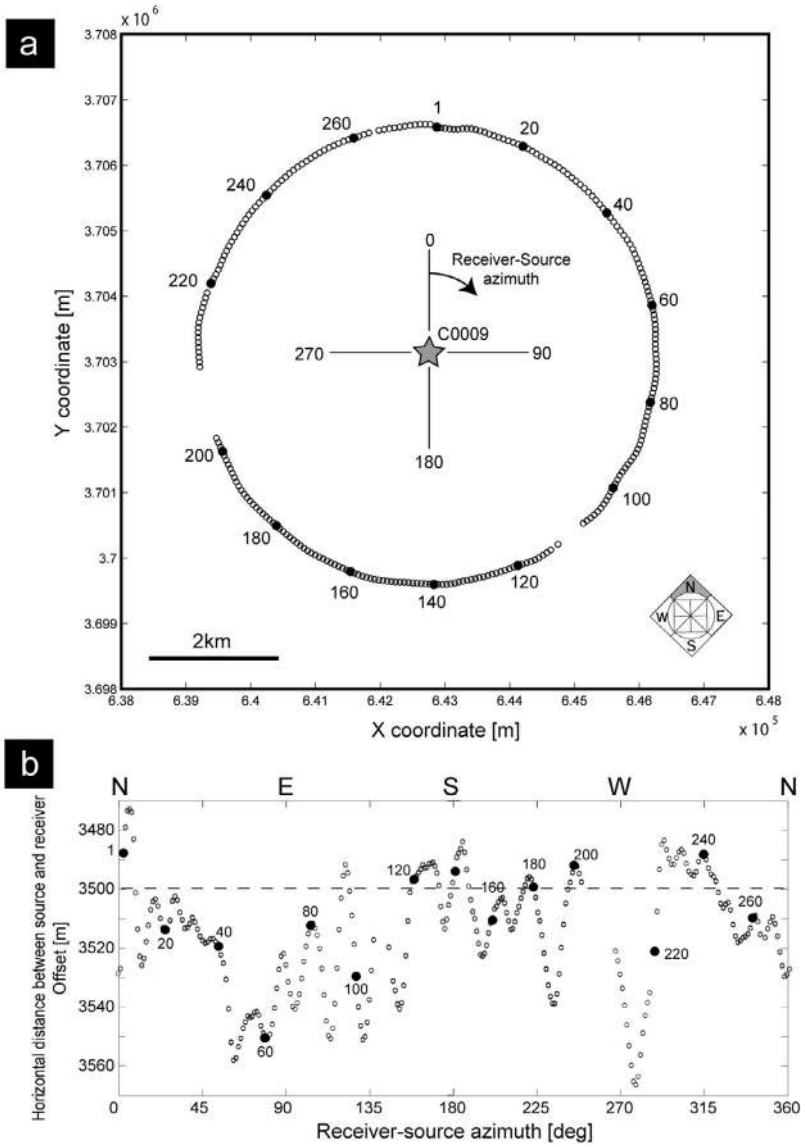

Figure 3. (a) Walkaround VSP survey geometry (plan view). Shooting proceeded in the clockwise direction. Star indicates borehole position. Numbers outside the shooting circle are FFID numbers (total of 278 shots). (b) Plot of horizontal offset (distance between source and receiver) versus receiver-source azimuth. The minimum and maximum offsets were 3472.88 and 3566.50 m, respectively.

this, we constructed a noise waveform using a band-pass filter of 25–30 Hz frequency range and subtracted it from the original waveform. Although this reduced the amplitude of the trace recorded by channel 10 compared to other channels, the less-noisy signal showed characteristics similar to those of the surrounding receivers, so we included the noise-reduced data from channel 10 in our anisotropic analyses.

[10] *Expedition 319 Scientists* [2010] defined four lithologic units (Units I–IV; Figure 4) at Site C0009 on the basis of geological, geophysical, and geochemical characteristics determined from cuttings, core, and wireline logs. On the basis of an abrupt downward increase in wood and lignite fragments and the occurrence of rounded grains of glauconite, they further divided Unit III into Subunits IIIA and IIIB. Subunit IIIB is characterized by lower Vp/Vs and higher resistivity than Subunit IIIA, and is therefore considered to be gas-enriched [*Doan et al.*, 2011]. Because the VSI tool was deployed across the boundary between Subunits IIIA and

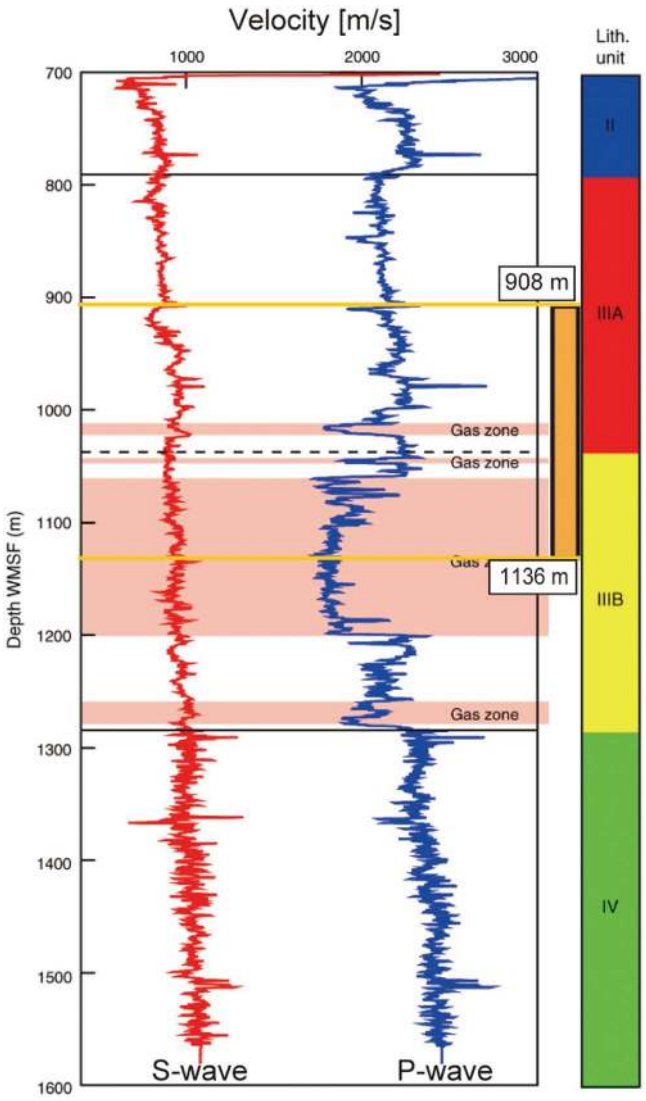

Figure 4. *Vp* and *Vs* estimated from downhole log data [*Saffer et al.*, 2009]. The interval where the VSI tool was deployed is indicated by the orange bar. Lithologic units defined by the *Expedition 319 Scientists* [2010] are also shown.

IIIB, it recorded data from the gas-enriched zone (Figure 4).

4. Methods and Results

4.1. Wavefield Separation

[11] To separate the various wavefields for seismic anisotropy analyses, we used information derived from orthogonal particle motions and moveout differences (Figure 2). First, the two raw horizontal components (X- and Y-axes) were rotated into radial and transverse components by examining the horizontal components of the particle motion of the direct *P* wave; the strongest amplitude of the direct *P* wave is parallel to the radial direction. The radial component lies in the plane containing the vertical receiver array and the shotpoint, and is roughly aligned with *P* waves and *SV* waves (Figure 2). The transverse component represents the *SH* wave.

[12] To estimate the incident angle of the direct *P* wave (Figure 2a), we applied hodogram analysis in the plane of the vertical and radial components. The hodogram analysis enabled us to accurately determine the incident angle for each receiver (60–70°). By using the incident angle determined at each receiver and applying a rotation of the vertical and radial components, we constructed the wavefield of the direct *P* waves (Figure 6).

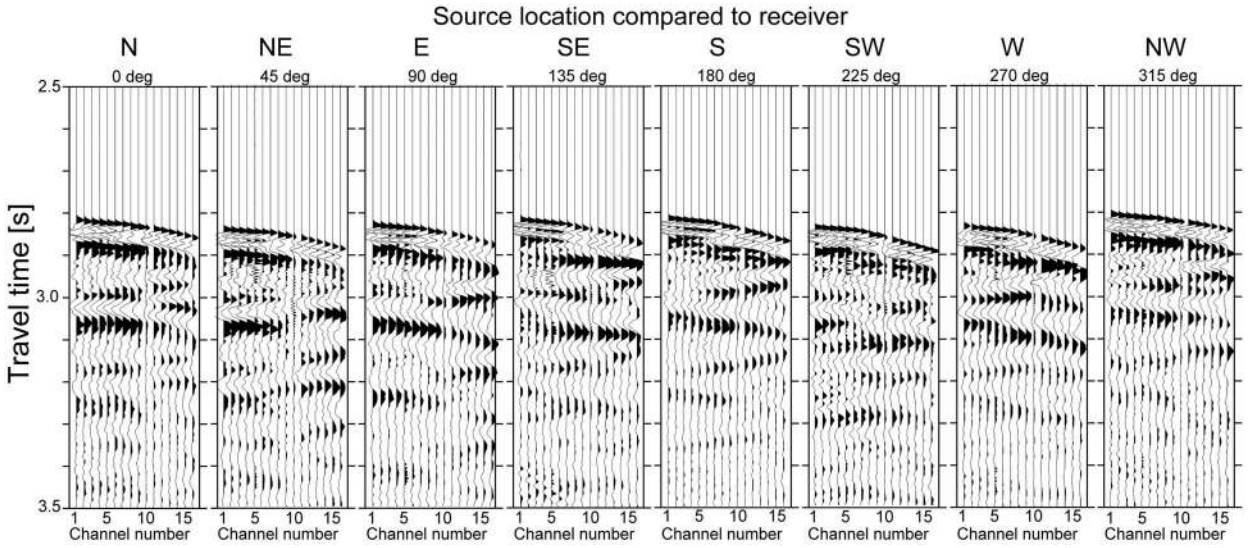

Figure 5. Examples of radial component records from walkaround VSP data displayed every 45°. Vertical axis indicates travel time in second. Horizontal axis indicates channel number (depth).

[13] Because the horizontal wavefields still included both the upgoing and downgoing waves, we needed to separate these wavefields before further analysis. We aligned the first break times of common shot gathers, and then applied an F–K filter to extract the upgoing wave. We then obtained the downgoing wave by subtracting the upgoing wave from the mixed wavefield.

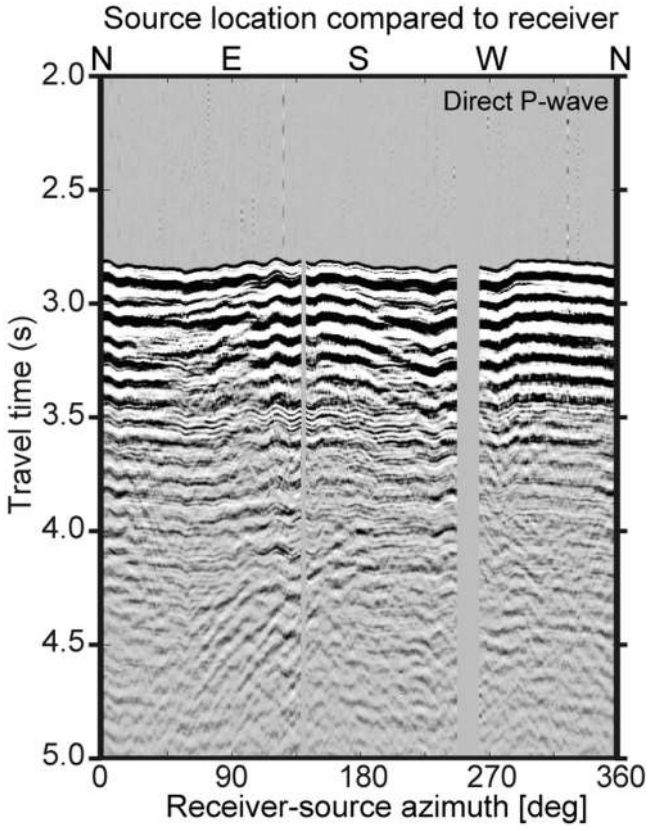

Figure 6. Direct *P* wave receiver gather from walkaround VSP data (channel 7). Horizontal axis indicates receiver-source azimuth (degree). The first-break time was used to estimate velocity anisotropy (open circles in Figure 7b). The maximum amplitude of the first arrival wavelet was used for analysis of amplitude variation with azimuth.

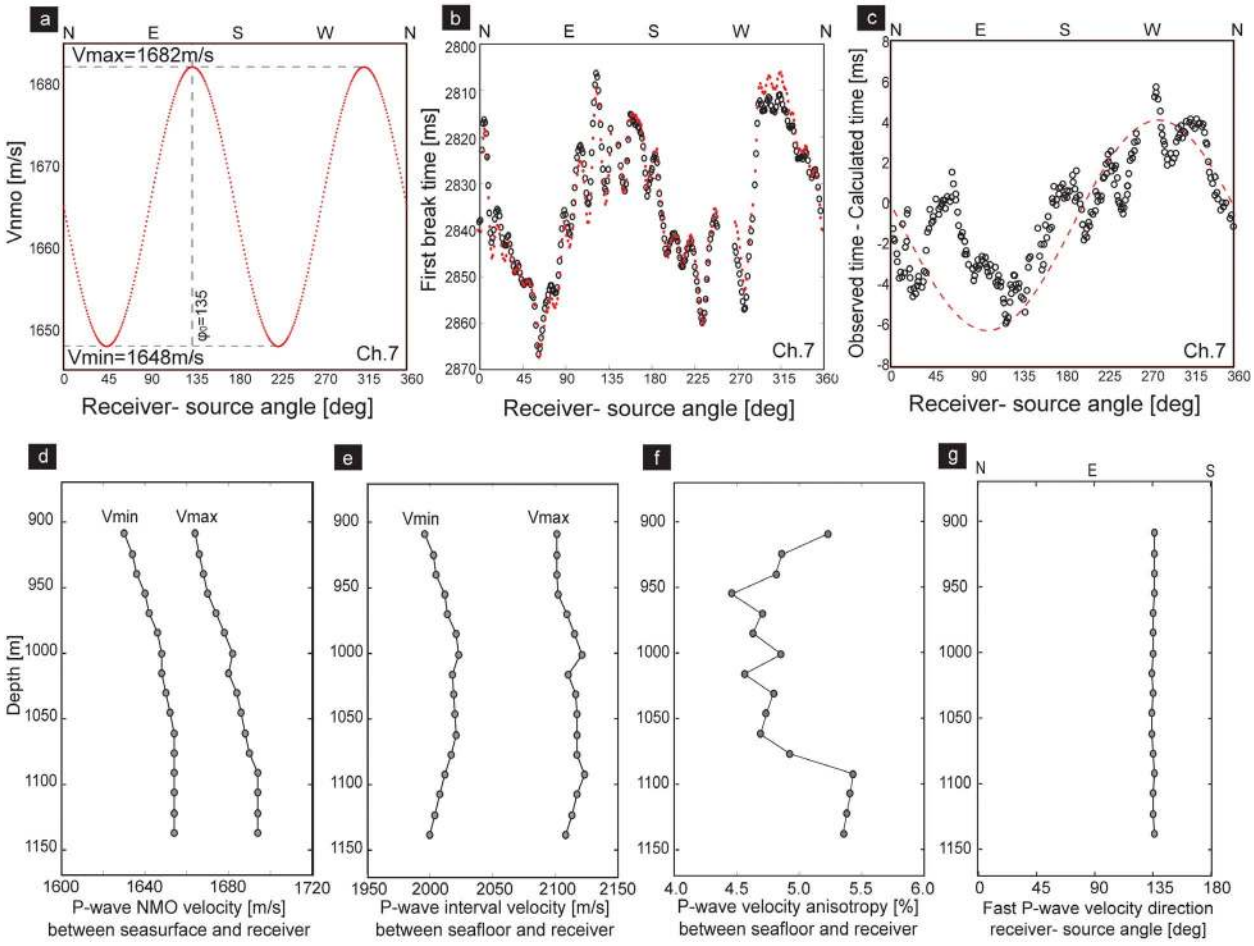

Figure 7. (a) Example of theoretical *P* wave velocity calculated from estimated anisotropic parameters by using equation (1). (b) Comparison of first-break time from field data (open circles) and first break time calculated from estimated anisotropic parameters using equation (2) (red small dots) plotted against receiver–source azimuth. We applied this analysis for all receivers. (c) Difference between observed and calculated travel time of Channel 7. (d) Maximum and minimum *P* wave NMO velocities between sea surface (shotpoints) and receivers. Vertical axis is depth below seafloor in meter. (e) Maximum and minimum *P* wave interval velocities within the sedimentary sequence (between seafloor and receivers). (f) *P* wave velocity anisotropy between the seafloor and receivers derived from velocities in Figure 7e. (g) Fast *P* wave velocity direction.

[14] We obtained several anisotropic parameters from the wavefields we separated from the walk-around VSP data (Figure 2b). From the wavefield of the direct *P* wave, we estimated (1) *P* wave velocity anisotropy by using azimuthal normal moveout (NMO) velocity analysis, and (2) *P* wave amplitude variation with azimuth by Fourier series fitting. From the wavefields of the radial and transverse horizontal components, we estimated (3) symmetry axes of *S* wave splitting.

4.2. *P* Wave Velocity Anisotropy

[15] To determine *P* wave velocity anisotropy, we performed elliptical-fitting analysis [*Grechka and Tsvankin*, 1998] for all receivers. The elliptical form allows the exact expression for NMO velocity to be determined from only three parameters: the velocities at the major and minor axes of the ellipse (i.e., maximum velocity $V_{\max}$ and minimum velocity $V_{\min}$) and the orientation of the ellipse relative to the coordinate axes (i.e., maximum velocity direction φ_0):

$$\frac{1}{V_{NMO}^2(\varphi)} = \frac{\cos^2(\varphi-\varphi_0)}{V_{\max}^2} + \frac{\sin^2(\varphi-\varphi_0)}{V_{\min}^2}, \qquad (1)$$

where $V_{NMO}(\varphi)$ is the NMO velocity parameterized by receiver-source direction (φ; radial direction; Figure 7a).

[16] The travel time (Figure 7b) can be calculated from the source–receiver horizontal offset x

(~3.5 km; Figure 3), zero-offset travel time t_0 derived from zero-offset VSP data, and $V_{NMO}(\varphi)$ calculated by equation (1):

$$t^2(x,\varphi) = t_0^2 + \frac{x^2}{V_{NMO}^2(\varphi)}. \quad (2)$$

Since we know t_0 and x in equation (2), we can calculate travel time $t(x, \varphi)$ for each shot from $V_{\max}$, $V_{\min}$, and φ_0. We estimated $V_{\max}$, $V_{\min}$, and φ_0 (Figures 7d and 7g) by fitting the calculated travel time to the observed arrival time of the downgoing direct *P* wave (Figure 6). Because the direct *P* wave is affected by noise much contained in vertical component, we applied a median filter to accurately determine the first break time.

[17] The estimated $V_{\max}$ and $V_{\min}$ represent NMO velocities between the sea surface and the receivers. From these NMO velocities (Figure 7d), we estimated interval velocities within the sedimentary sequence (between seafloor and receiver) by using the Dix equation (Figure 7e) [*Yilmaz and Doherty*, 2001], which showed that interval velocities within the sedimentary sequence varied by ~110 m/s. This corresponds to ~5% velocity anisotropy (Figure 7f). The azimuth of the fast *P* wave velocity direction φ_0 is about 135° (Figure 7g), which corresponds to the subduction direction of the Philippine Sea plate.

[18] At depths greater than 1068 m below seafloor, interval velocities in the sequence between the seafloor and receivers decreased with increasing depth (Figure 7e). This interval of decreasing interval velocity corresponds to the gas-enriched zone (Figure 4) and indicates that the presence of gas may significantly decrease the *P* wave velocity. *P* wave velocity anisotropy (Figure 7f) further increase in the gas-enriched zone.

[19] The estimated azimuthal velocity difference would be expected to be affected by seafloor depth variation. The maximum difference in seafloor depth within the shooting circle is 25 m, which gives an estimated error due to seafloor depth difference of ~4 ms in travel time. Because the maximum *P* wave travel time difference derived from the HTI anisotropy (Figure 7a) was ~50 ms, differences of seafloor depth did not significantly affect our estimates of velocity anisotropy.

[20] Because we found a good fit between observed and calculated travel times (Figure 7b), it is clear that the dip of the Kumano basin sequence (tilted transverse isotropy; TTI) had little effect on the estimated anisotropic properties. The small difference between observed and calculated travel time (Figure 7c) can be partially explained by the dip of the Kumano basin sequence. If the effect of dip of sedimentary sequence is dominant, a sinusoidal curve of 2π period would be expected. In fact, the residual between observed and calculated travel time (Figure 7c) indicate landward dipping sedimentary sequence, because the observed travel time is shorter than the calculated time for a receiver-source angle of 100 degree (updip direction of the strata; Figure 7c) and because *P* wave velocity for layer-parallel direction is faster than that for layer-normal direction [*Hudson*, 1981]. However, the influence of the layer dipping effect on the travel time variation is small (<10 ms) compared to the fracture-related (or grain-contact related) HTI anisotropy, and is similar in magnitude to the error derived from seafloor depth difference (~4 ms).

[21] The horizontal *P* wave velocity anisotropy measured on core samples from the same borehole scatters in a range of ±10% or even larger [*Expedition 319 Scientists*, 2010]. We believe that the anisotropy difference between VSP (~5%) and laboratory measurements (±10%) is due to different scale as well as different stress conditions during measurement. Our estimated anisotropy using low frequency source signal (several 10 Hz) is averaged along the raypath from seafloor to receivers. On the other hand, the velocities of core samples could be affected by small-scale cracks formed or opened during stress unloading. Furthermore core samples were obtained from deeper lithology, which may have more fractures and stronger anisotropy compared to unconsolidated shallower sediment.

4.3. *P* Wave Amplitude Variation With Azimuth

[22] Although *P* wave velocities can be determined only with low spatial resolution, we can reveal anisotropic characteristics at higher resolution by using amplitude information. The strong amplitude direction should be aligned parallel to fracture (or crack) orientation. For this analysis, we focused on the amplitude variation of first arrival wavelets of direct *P* waves (Figure 8). We aligned all traces at the first break time and extracted the maximum amplitude of the first arrival signal wavelet (Figure 8a).

[23] Elliptical fitting analysis can be used to determine amplitude variations in an HTI medium (e.g., equation (1)); however, we observed high- and low-frequency amplitude variations that suggest we were dealing with mixed fracture orientations as well as a dipping sedimentary sequence. To characterize amplitude variations including several frequency

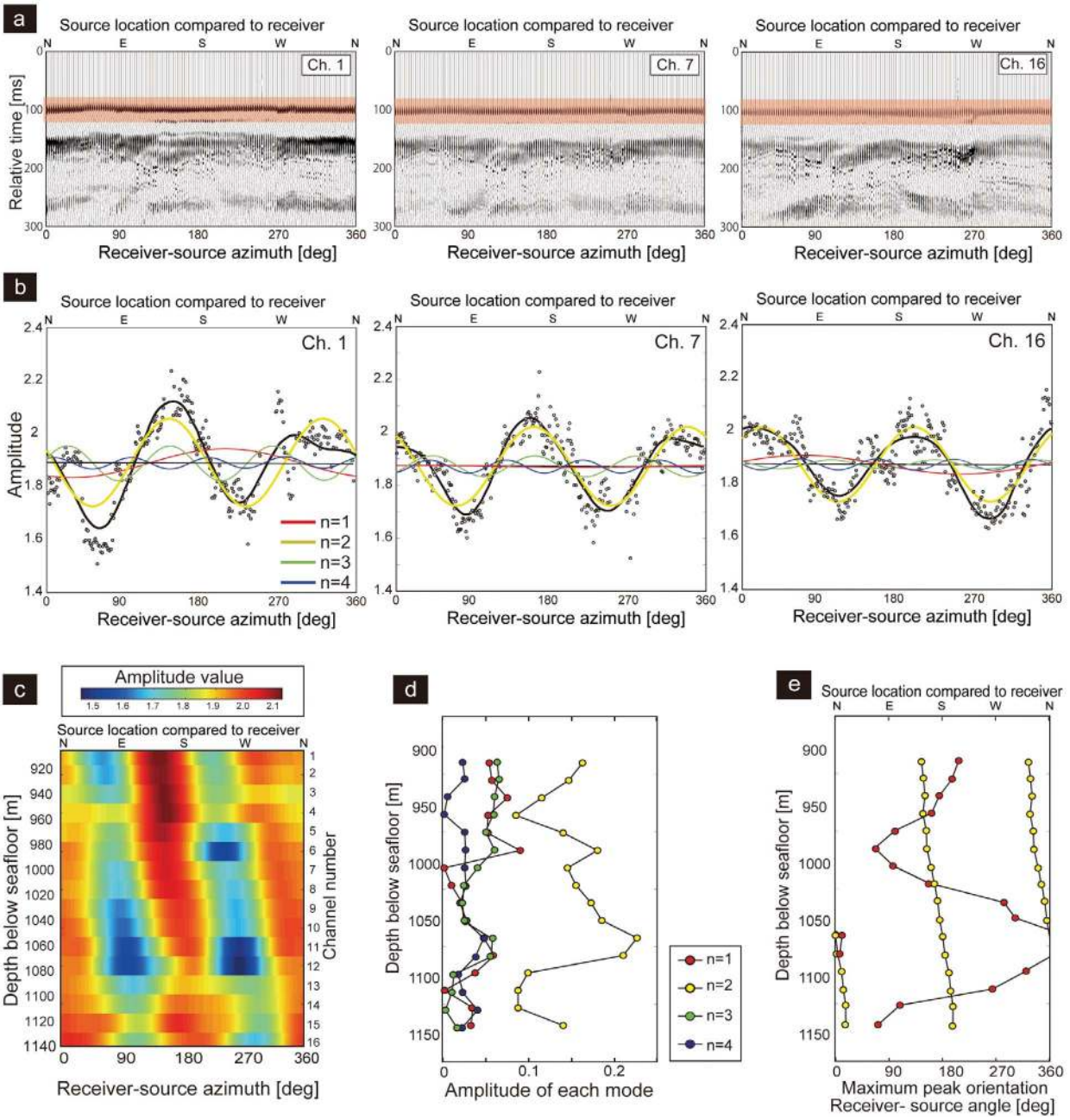

Figure 8. (a) Examples of enlarged displays of representative first-arrival waveforms (Channels 1, 7, 16). Horizontal axis indicates the receiver-source azimuth. Red band indicates search area for maximum amplitude. (b) Examples of first-break amplitude variation with azimuth (dots). Thick black curve is smoothed amplitude variation. Colored curves indicate Fourier series fitting. (c) Depth profile of first-break amplitude variation with azimuth. Warmer color indicates strong amplitude. The amplitude variation corresponds to the black curves in Figure 8b. (d) Depth profile of amplitude of Fourier series; A_1, A_2, A_3, A_4 in equation (3). (e) Depth profile of phase of Fourier series; φ_1 and φ_2 in equation (3).

components, we used the Fourier series of azimuths [*Ikelle and Amundsen*, 2001]:

$$R(\varphi) = F_0 + \sum_{n=1}^{4}[F_n \cos(n\varphi) + G_n \sin(n\varphi)] = \sum_{n=0}^{4} A_n \cos n(\varphi - \varphi_n), \quad (3)$$

where $A_n = \sqrt{F_n^2 + G_n^2}$. The phase of each frequency mode n is calculated as $\varphi_n = \arctan(G_n/F_n)/n$. We determined F_0, F_n, and G_n by least squares fitting to the extracted maximum amplitude variation (Figure 8b). This analysis allowed us to reveal the overall trend of amplitude variation with

azimuth (smoothed amplitude variation; Figure 8c) as well as the characteristics of each frequency component *n* (Figures 8d and 8e).

[24] From the smoothed amplitude variation with azimuth (Figure 8c), we observed strong amplitudes from 135° to 150° in the shallow section (910–990 m below seafloor), which is almost the same as the azimuth of the fast *P* wave velocity (Figure 7g). However, deeper in the section (990–1130 m below seafloor), we observed that the azimuth of the strong amplitudes rotated clockwise with depth from 150° to 180° (Figure 8c).

4.4. *S* Wave Splitting

[25] When an *S* wave propagates through an anisotropic elastic solid, it splits into two perpendicular polarizations that travel with different velocities [*Crampin*, 1981]. We observed the *S* wave splitting in both the up- and downgoing converted *S* waves. The amplitude of the radial component was fairly constant with azimuth (Figures 9a, 9c, and 9e), whereas the transverse component exhibited considerable variations of amplitude with azimuth and a polarity reversal every 90° (Figures 9b, 9d, and 9f). At the polarity reversal, the amplitude of the transverse component passed through zero at 45° and 135° (Figure 9f); these azimuths correspond to the principal symmetry axes of the anisotropic medium.

[26] The transverse-component behavior is clearly observed on the transverse to radial energy ratio (Figure 10) [*Garotta and Granger*, 1988; *Maultzsch et al.*, 2009]. We identified clear minimum energy of transverse components for the principal symmetry axes (45° and 135°). The directions of symmetry axes are constant for depth direction (Figure 10). The orientations of these axes correspond to the polarization directions of the fast and slow *S* waves [*Gaiser*, 1999]. Since the direction of the fast *P* wave velocity was 135°, the direction of the fast *S* wave polarization should also be 135°. Therefore, the axes (135°) correspond to the strike of the fracture or stress-induced crack [*Crampin*, 1985].

[27] The observed downgoing *SV* waves were converted from *P* waves at geological boundaries shallower than the receivers (e.g., the seafloor). *SH* waves are generated from *SV* waves at geological boundaries between the seafloor and the receivers. The zero-amplitude band of the transverse component (Figure 9b) indicate that the first arrivals of downgoing *S* waves are converted from *P* wave within the sedimentary sequence (beneath the seafloor); *S* waves converted at the seafloor should have later arrival times than the observed first arrivals of the *PS* converted waveform. From the *Vp*/*Vs* ratio (Figure 4), we estimated that the *S* wave converted at the seafloor arrived ~0.7 s later than the first arrival of the direct *P* wave (black arrows in Figure 9e). The *S* wave converted at the seafloor appears in walkaway VSP data as the strongest *PS* converted waveform.

[28] In Figure 9e (radial component), the velocity of *PS* converted waveform looks slower (longer travel time) for the interpreted fast *S* wave polarization direction (135°). However, since Figure 9e is aligned by first arrivals of direct *P* wave, the *PS* converted wave is displayed slower for the fast *P* wave polarization direction. Yellow sinusoidal curve in Figure 9e indicates travel time variation due to *P* wave velocity anisotropy (~5%). The agreement between sinusoidal curvature of *P* wave velocity anisotropy (yellow curve in Figure 9e) and the *PS* wave converted at the seafloor (black arrow in Figure 9e) indicate that the sinusoidal curvature observed in radial component is almost explained by *P* wave velocity anisotropy (Figure 7).

[29] For the upgoing *S* wave, it is difficult to identify the conversion surface, although the converted *S* wave could be seen in the walkaway VSP data. Therefore we did not estimate S-wave velocity anisotropy from the upgoing *S* wave in this study.

5. Discussion

5.1. Principal Horizontal Stress Orientation

[30] The anisotropic directions estimated from our VSP analysis are consistent with the maximum horizontal stress orientations estimated by *Lin et al.* [2010] from borehole breakouts (red and blue bars in Figure 11). Therefore, the seismic anisotropy we detected has been indicated the orientation of the principal stresses. The stress-induced anisotropy is frequently explained by alignment of stress-induced cracks, or the closure of randomly distributed cracks in response to increased stress [*Hudson*, 1981]. Accurately, seismic anisotropy within the unconcolidated sediment (i.e., Kumano basin) could be generated mainly by increasing contact between grains [*Johnson et al.*, 1998]. However, grain-contact model have similar characteristics with crack model when we consider the azimuthal seismic anisotropy.

[31] These directions of anisotropy obtained in this study are compatible with the fast *S* wave polarization

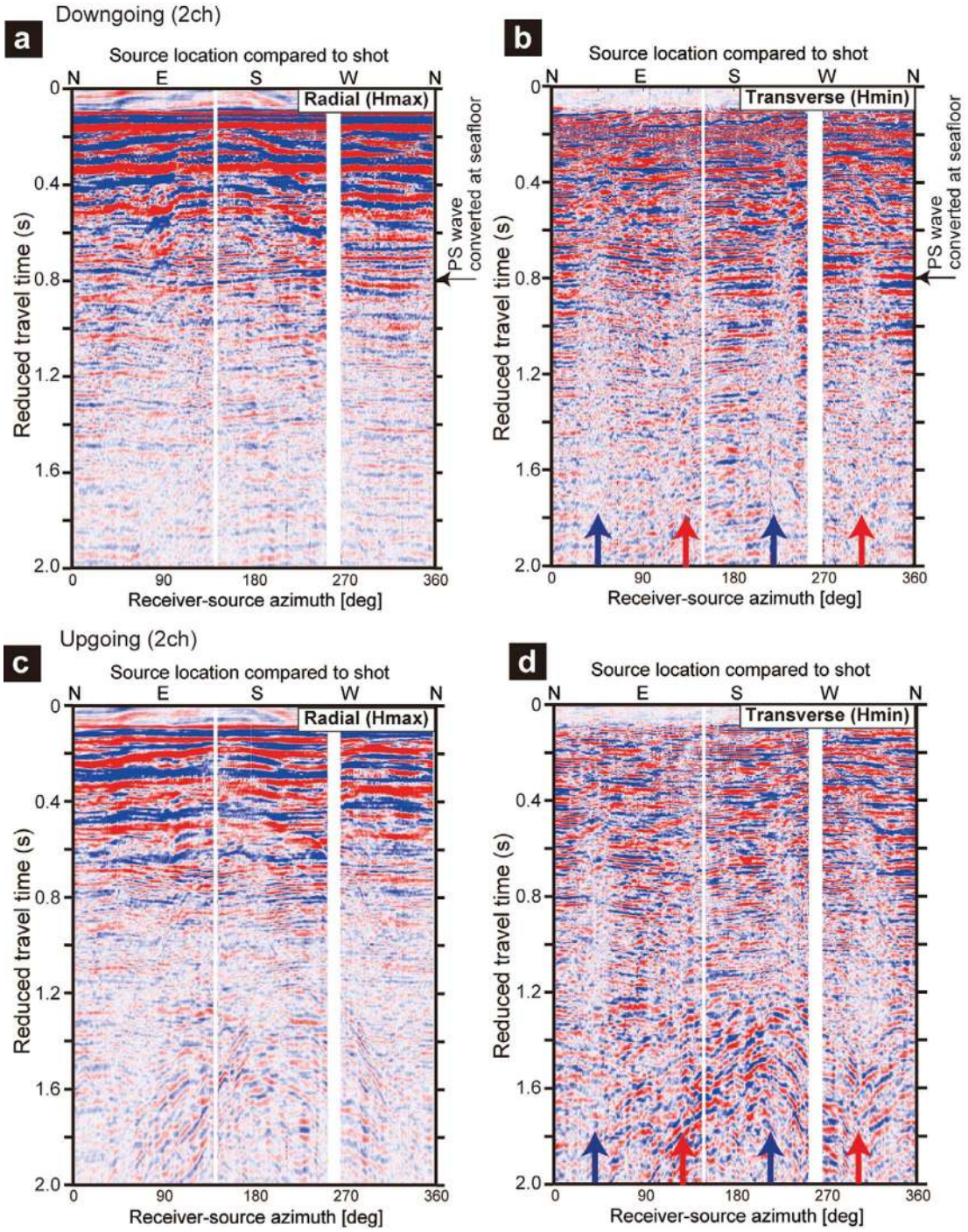

Figure 9. (a–d) Examples of azimuthal amplitude variation of radial and transverse components of upgoing and downgoing split *S* waves (Channel 2). These profiles are aligned with first-break time at 100 ms. Red and blue arrows indicate zero-amplitude bands that correspond to fast- and slow-polarization directions. The interpreted *PS* wave converted at the seafloor is indicated by black arrows. These profiles indicate that the *S* waves are converted from *P* waves beneath the seafloor, because zero-amplitude bands are identified before the arrival of *PS* waves converted at the seafloor. Enlarged (e) radial and (f) transverse components of downgoing split *S* waves. These profiles are corresponding to the interval of 0.6–1 s of Figures 9a and 9b. Yellow sinusoidal curvature in Figure 9e indicates travel time variation due to *P* wave velocity anisotropy. The agreement between sinusoidal curvature of the *P* wave anisotropy (yellow curve) and the *PS* converted waveforms (black arrows) indicates that the sinusoidal curvature of *PS* converted waveform is derived from *P* wave velocity anisotropy (not from *S* wave velocity anisotropy). Yellow box in Figure 9f indicates polarity reversal across the symmetry axes.

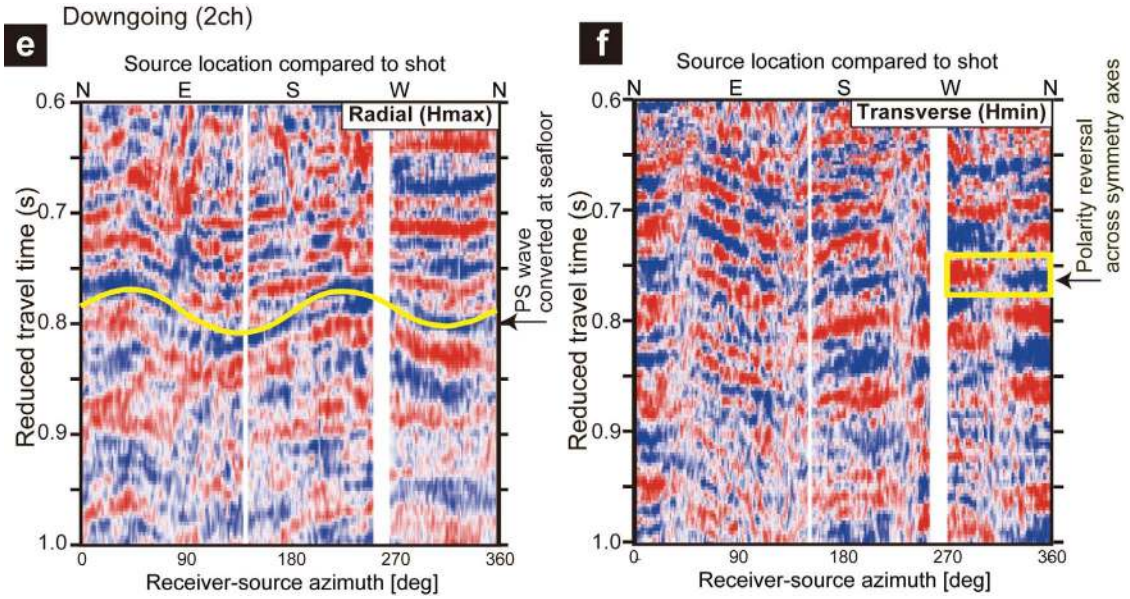

Figure 9. (continued)

directions estimated by *Tsuji et al.* [2011] from active-source wide-angle data recorded by ocean bottom seismometer (OBS) (gray bars in Figure 11). In details, the fast *S* wave polarization directions derived from OBS analysis is more perpendicular to the subduction direction of Philippine Sea plate around Site C0009. Since the fast *S* wave polarization directions from OBS analysis indicate average anisotropic properties between the seafloor and the plate interface [*Tsuji et al.*, 2011], the difference between these directions of anisotropy may indicate that the fractures within accretionary prism (beneath the Kumano basin) are developed for the subduction perpendicular direction.

[32] We do not have a clear explanation for the strong *P* wave amplitude direction in the deeper part of the sequence (~180°; Figure 8). The orientation of the fractures may have changed locally within the interval investigated by the VSI tool, since the anisotropic characteristics at higher resolution can be extracted by using amplitude information. Furthermore there is a possibility that the fractures associated with ancient (and therefore different) stress conditions in deeper lithology influence to the estimated amplitude anisotropy. The deeper lithology should be more influenced by deformation within the accretionary prism beneath the Kumano basin. Actually, in the deep interval (1090–1150 m below seafloor), the amplitude variation with azimuth of the $n = 2$ frequency component is relatively small (Figure 8d), which indicates some mixed fracture orientations. This interpretation for the amplitude anisotropy is similar to that for the variation in orientation between VSP-derived anisotropy, reflecting elastic properties of fore-arc basin sediments, and OBS-derived anisotropy (Figure 11), reflecting elastic properties over a broader depth interval, as described above.

5.2. Horizontal Differential Stress

[33] We estimated the magnitude of horizontal differential stress from the estimated *P* wave velocity anisotropy (Figure 7), because amount of stress-induced cracks (or degree of grain contact) has a relation with magnitude of differential stress and can be revealed from the degree of seismic anisotropy. The laboratory measurements for the rock samples obtained in this study area [*Hashimoto et al.*, 2010; *Raimbourg et al.*, 2011; *Tsuji et al.*, 2008] demonstrated that the gradient of the *P* wave velocity–effective stress relationship $\partial V_p/\partial\sigma'$ were 20~40 m/s/MPa in elastic domain, although the relationship was nonlinear. The gradient of velocity–stress relationship of these laboratory data is consistent with the results of a laboratory experiment by *Zimmer et al.* [2002] who showed that the *P* wave velocity gradient in unconsolidated sediment was ~30 m/s/MPa for an effective pressure range 0–10 MPa. Therefore, we assume that the upper and lower bound of velocity-stress gradient is 20 m/s/MPa and 40 m/s/MPa respectively. Here

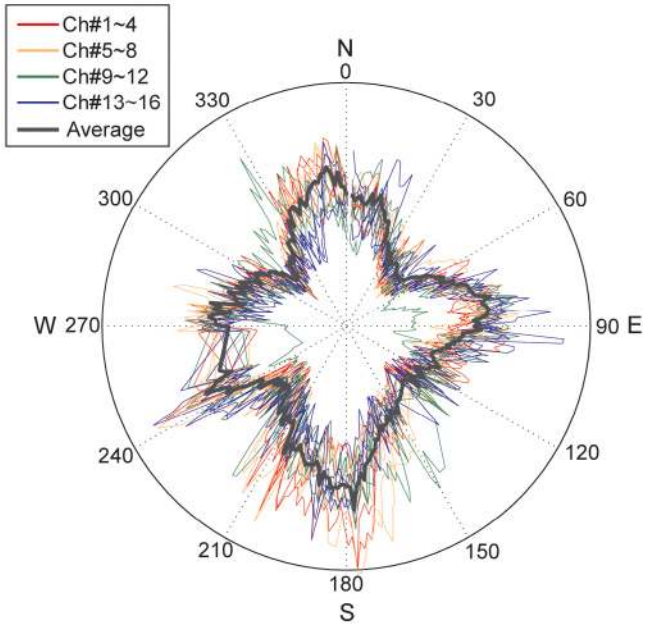

Figure 10. Rose plot of the transverse to radial energy ratio measured from the walkaround VSP data. The results for each individual receiver level and the average are displayed. We used downgoing waveform around PS wave converted at the seafloor. There are two clear minima in the energy ratio at orthogonal azimuths around 45° and 135°.

we assume that these velocity gradients are derived from closure of randomly oriented cracks or grain-contact increasing [*Tsuji et al.*, 2008].

[34] If we can apply the velocity-stress relationship $\partial V_p/\partial\sigma' = 20\sim40$ m/s/MPa for horizontal direction ($\partial V_p/\partial\sigma' = \partial V_p/\partial\sigma'_h$) because of the assumption of randomly oriented cracks, we estimate horizontal differential stress to be 2.7~5.5 MPa by using our estimated P wave velocity anisotropy (ΔVp = 110 m/s; Figure 7e) in the following equation:

$$\sigma_{H\max} - \sigma_{H\min} = \Delta V_p \frac{\partial\sigma'_h}{\partial V_p}. \quad (4)$$

The estimated P wave velocity anisotropy is an NMO-derived velocity anisotropy, which is not the same as a horizontal velocity anisotropy. However, because the incident angle of our relatively wide-offset data (~3.5 km) was 60–70°, our estimated velocity should not differ greatly from the horizontal velocity.

[35] In our estimation of differential stress, we assumed that differential stress was constant between the seafloor and the receiver, because the estimated interval velocity as well as anisotropy is averaged value between seafloor and receiver. However, the differential stress could be small close to the seafloor, so our assumption minimizes the estimated horizontal differential stress in deep lithology.

5.3. Maximum Horizontal Stress

[36] According to a hydraulic fracturing packer test at Site C0009, *Saffer et al.* [2009] estimated the difference between the minimum horizontal and vertical stresses to be a few megapascals at depth around the VSI tool deployed interval (Figure 12). This stress difference is similar to (or a little smaller than) the difference between the maximum and minimum horizontal stresses estimated in this study (2.7~5.5 MPa), and indicates that maximum horizontal stress $\sigma_{H\max}$ is similar to (or a little larger than) the vertical stress σ_v at Site C0009 (Figure 12). Therefore, we can roughly estimate the maximum horizontal stress, which is normally most difficult to determine among the three principal stress components.

[37] Although previous studies indicated normal fault regime within the Kumano basin seaward of our study area (Site C0002) [*Byrne et al.*, 2009; *Chang et al.*, 2010], our estimated results (Figure 12) indicate normal to strike-slip regime at Site C0009. Because our study area (Site C0009) is located further landward from the Site C0002, the stress state within the Kumano basin would be changed from normal regime near the mega-splay fault

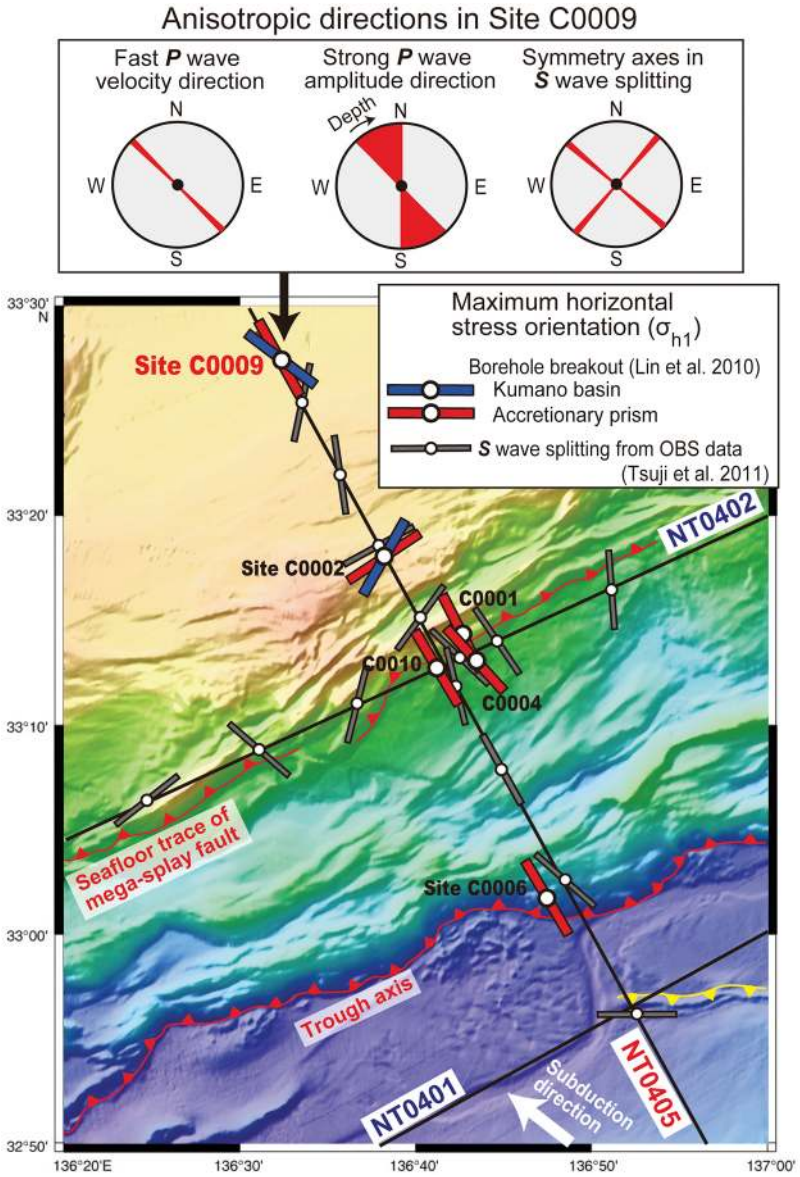

Figure 11. Comparison of the directions estimated from fast *P* wave velocity, strong *P* wave amplitude, principal axis of *S* wave splitting, and previously estimated principal horizontal stress orientations. Red and blue bars indicate principal horizontal stress estimated from borehole breakouts by *Lin et al.* [2010]. Blue bars indicate principal horizontal stress within the Kumano basin. Gray bars indicate the fast *S* wave polarization direction estimated from OBS data by *Tsuji et al.* [2011]. Yellow line seaward of the trough axis shows fault induced by intraoceanic fault displacement [*Tsuji et al.*, 2009].

(Site C0002) to strike-slip regime in landward region (Site C0009).

6. Summary

[38] We summarize here the main results obtained in this study:

[39] 1. We showed that *P* wave interval velocity anisotropy within the sediments of the Kumano basin at depths of less than 908 m below the seafloor is ~5%. The fast *P* wave velocity direction is aligned with the convergence vector of the Philippine Sea plate (135°).

[40] 2. From the amplitude of the direct *P* wave, we revealed anisotropic characteristics with high resolution. The azimuth of the strong amplitude direction is 135° in the shallow sequence and is consistent with the azimuth of the fast *P* wave

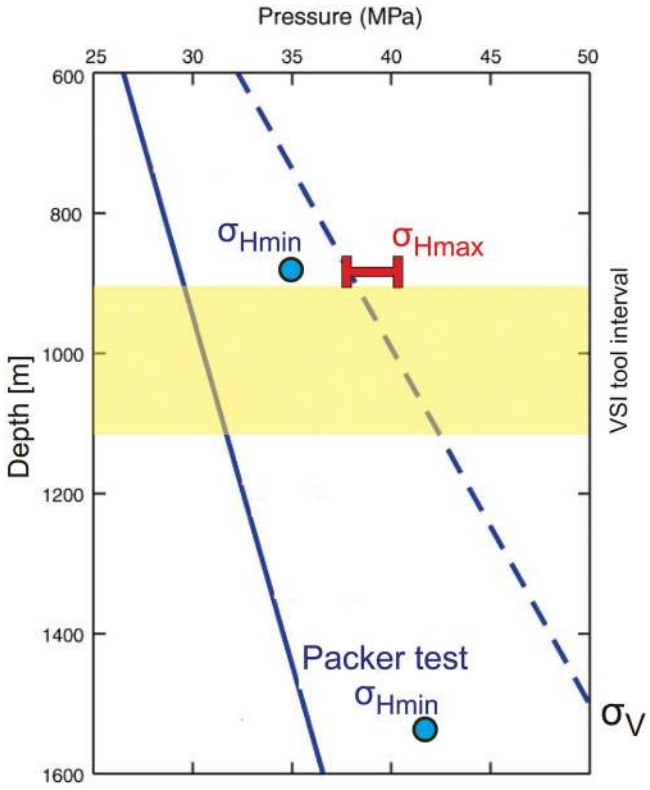

Figure 12. Pressure and stress profile around the interval where the VSI tool was deployed [*Saffer et al.*, 2009]. Blue solid line indicates hydrostatic pressure. Blue dashed line indicates vertical stress estimated from density information. Blue circles indicate minimum horizontal stress estimated from hydraulic fracturing packer tests. Red bar indicates the maximum horizontal stress estimated from *P* wave velocity anisotropy.

velocity direction (and the direction of plate subduction). However, the azimuth of the strong amplitude direction is 180° in the deep sequence, perhaps because of local changes to fracture orientation or existence of ancient fractures.

[41] 3. For the transverse components, we observed principal symmetry axes of *S* wave splitting (zero amplitude bands) every 90°. The principal axes of symmetry for *S* wave splitting are 45° and 135°.

[42] 4. We observed similar anisotropic orientations for the fast *P* wave velocity direction, the strong *P* wave amplitude direction, and the principal axes of symmetry for *S* wave splitting. These anisotropic orientations are consistent with previously estimated maximum horizontal stress orientations (i.e., plate subduction direction).

[43] 5. The horizontal differential stress determined from *P* wave velocity anisotropy (~110 m/s) was estimated to be 2.7~5.5 MPa, indicating that the maximum horizontal stress is similar to (or a little larger than) the vertical stress.

[44] 6. This study demonstrates that walkaround VSP data provide useful information (i.e., anisotropic properties) for characterization of stress orientation and magnitude even in unconsolidated sediment. This analysis gives insight to monitoring dynamic stress state around the seismogenic faults using borehole seismometers and artificial source.

Acknowledgments

[45] We thank the scientists and crew of IODP Expedition 319, especially to co-chief scientists D. Saffer, L. McNeill and T. Byrne, and staff scientists S. Toczko, N. Eguchi and K. Takahashi. VSP data were provided by IODP and IFREE/JAMSTEC for this research. We thank C. Chang, an anonymous reviewer, and the associate editor for constructive comments. Seismic data processing was supported by JGI Inc. We are especially grateful to N. Aoki (JGI Inc.) for the data processing. T. Tsuji was supported by the Grant-in-Aid for Young Scientists (B) program from the Japan Society for the Promotion of Science (JSPS) (20760568), the JSPS Excellent Young Researcher Visit Program (21–5338), and Grant-in-Aid for Scientific Research on Innovative Areas (21107003).

References

Ando, M. (1975), Source mechanisms and tectonic significance of historical earthquakes along the Nankai Trough, *Tectonophysics*, *27*, 119–140, doi:10.1016/0040-1951(75)90102-X.

Bangs, N. L., T. H. Shipley, S. Gulick, G. Moore, S. Kuramoto, and Y. Nakamura (2004), Evolution of the Nankai Trough décollement from the Trench into the seismogenic zone: Inferences from three-dimensional seismic reflection imaging, *Geology*, *32*, 273–276, doi:10.1130/G20211.2.

Byrne, T. B., W. Lin, A. Tsutsumi, Y. Yamamoto, J. C. Lewis, K. Kanagawa, Y. Kitamura, A. Yamaguchi, and G. Kimura (2009), Anelastic strain recovery reveals extension across SW Japan subduction zone, *Geophys. Res. Lett.*, *36*, L23310, doi:10.1029/2009GL040749.

Chang, C., L. C. McNeill, J. C. Moore, W. Lin, M. Conin, and Y. Yamada (2010), In situ stress state in the Nankai accretionary wedge estimated from borehole wall failures, *Geochem. Geophys. Geosyst.*, *11*, Q0AD04, doi:10.1029/2010GC003261.

Crampin, S. (1981), A review of wave motion in anisotropic and cracked elastic media, *Wave Motion*, *3*, 343–391, doi:10.1016/0165-2125(81)90026-3.

Crampin, S. (1985), Evaluation of anisotropy by shear-wave splitting, *Geophysics*, *50*, 142–152, doi:10.1190/1.1441824.

Crampin, S., Y. Gao, and S. Peacock (2008), Stress-forecasting (not predicting) earthquakes: A paradigm shift?, *Geology*, *36*, 427–430, doi:10.1130/G24643A.1.

Doan, M.-L., M. Conin, P. Henry, T. Wiersberg, D. Boutt, D. Buchs, D. Saffer, L. C. McNeill, D. Cukur, and W. Lin (2011), Quantification of free gas in the Kumano fore-arc basin detected from borehole physical properties: IODP NanTroSEIZE drilling Site C0009, *Geochem. Geophys. Geosyst.*, *12*, Q0AD06, doi:10.1029/2010GC003284.

Expedition 319 Scientists (2010), Site C0009 in *NanTroSEIZE Stage 2: NanTroSEIZE Riser/Riserless Observatory*, *Proc. Integr. Ocean Drill. Program*, *319*, doi:10.2204/iodp.proc.319.103.2010.

Gaiser, J. E. (1999), Applications for vector coordinate systems of 3-D converted-wave data, *Lead. Edge*, *18*, 1290–1300, doi:10.1190/1.1438202.

Garotta, R., and P. Y. Granger (1988), Acquisition and processing of 3C × 3D data using converted waves, paper presented at 58th SEG Meeting, Anaheim, Calif.

Grechka, V., and I. Tsvankin (1998), 3-D description of normal moveout in anisotropic inhomogeneous media, *Geophysics*, *63*, 1079–1092, doi:10.1190/1.1444386.

Gulick, S., N. Bangs, G. Moore, J. Ashi, K. Martin, D. Sawyer, H. J. Tobin, S. Kuramoto, and A. Taira (2010), Rapid forearc basin uplift and megasplay fault development from 3D seismic images of Nankai Margin off Kii Peninsula, Japan, *Earth Planet. Sci. Lett.*, *300*, 55–62, doi:10.1016/j.epsl.2010.09.034.

Haacke, R. R., and G. K. Westbrook (2006), A fast, robust method for detecting and characterizing azimuthal anisotropy with marine PS converted waves, and its application to the west Svalbard continental slope, *Geophys. J. Int.*, *167*, 1402–1412, doi:10.1111/j.1365-246X.2006.03186.x.

Haacke, R. R., G. K. Westbrook, and S. Peacock (2009), Layer stripping of shear-wave splitting in marine PS waves, *Geophys. J. Int.*, *176*, 782–804, doi:10.1111/j.1365-246X.2008.04060.x.

Hashimoto, Y., H. J. Tobin, and M. Knuth (2010), Velocity–porosity relationships for slope apron and accreted sediments in the Nankai Trough Seismogenic Zone Experiment, Integrated Ocean Drilling Program Expedition 315 Site C0001, *Geochem. Geophys. Geosyst.*, *11*, Q0AD05, doi:10.1029/2010GC003217.

Hudson, J. A. (1981), Wave speeds and attenuation of elastic waves in material containing cracks, *Geophys. J. R. Astron. Soc.*, *64*, 133–150.

Ikelle, L. T., and L. Amundsen (2001), AVO-A response of an anisotropic half-space for P-P, P-SV and P-SH data, in *Proceedings of the Ninth International Workshop on Seismic Anisotropy (9IWSA)*, edited by L. Ikelle and A. Gangi, pp. 77–106, Soc. of Explor. Geophys., Tulsa, Okla.

Johnson, D. L., L. M. Schwartz, D. Elata, J. G. Berryman, B. Hornby, and A. N. Norris (1998), Linear and nonlinear elasticity of granular media: Stress-induced anisotropy of a random sphere pack, *J. Appl. Mech.*, *65*, 380–388, doi:10.1115/1.2789066.

Kaneshima, S., M. Ando, and S. Kimura (1988), Evidence from shear-wave splitting for the restriction of seismic anisotropy to the upper crust, *Nature*, *335*, 627–629, doi:10.1038/335627a0.

Kikuchi, M., M. Nakamura, and K. Yoshikawa (2003), Source rupture processes of the 1944 Tonankai earthquake and the 1945 Mikawa earthquake derived from low-gain seismograms, *Earth Planets Space*, *55*, 159–172.

Kinoshita, M., H. J. Tobin, M. K. Thu, and the Expedition 314 Scientists (2008), NanTroSEIZE Stage1A: NanTroSEIZE LWD Transect, *Integr. Ocean Drill. Program Prelim. Rep.*, *314*, doi:10.2204/iodp.pr.314.2008.

Leggett, J. K., Y. Aoki, and T. Toba (1985), Transition from frontal accretion to underplating in a part of the Nankai Trough Accretionary Complex off Shikoku (SW Japan) and extensional features on the lower trench slope, *Mar. Pet. Geol.*, *2*, 131–142.

Lin, W., et al. (2010), Present-day principal horizontal stress orientations in the Kumano forearc basin of the southwest Japan subduction zone determined from IODP NanTroSEIZE drilling Site C0009, *Geophys. Res. Lett.*, *37*, L13303, doi:10.1029/2010GL043158.

Loveless, J. P., and B. J. Meade (2010), Geodetic imaging of plate motions, slip rates, and partitioning of deformation in Japan, *J. Geophys. Res.*, *115*, B02410, doi:10.1029/2008JB006248.

Maultzsch, S., R. Nawab, S. Yuh, M. Idrees, and B. Frignet (2009), An integrated multi-azimuth VSP study for fracture characterization in the vicinity of a well, *Geophys. Prospect.*, *57*, 263–274, doi:10.1111/j.1365-2478.2008.00769.x.

Mavko, G., T. Mukerji, and J. Dvorkin (1998), *The Rock Physics Handbook, Tool for Seismic Analysis in Porous Media*, Cambridge Univ. Press, Cambridge, U. K.

Moore, G. F., T. H. Shipley, P. L. Stoffa, D. E. Karig, A. Taira, S. Kuramoto, H. Tokuyama, and K. Suyehiro (1990), Structure of the Nankai Trough accretionary zone from multichannel seismic reflection data, *J. Geophys. Res.*, *95*, 8753–8765, doi:10.1029/JB095iB06p08753.

Moore, G. F., et al. (2009), Structural and seismic stratigraphic framework of the NanTroSEIZE Stage 1 transect, in *NanTroSEIZE Stage 1: Investigations of Seismogenesis, Nankai Trough, Japan*, *Proc. Integr. Ocean Drill. Program*, *314/315/316*, doi:10.2204/iodp.proc.314315316.102.2009.

Park, J.-O., T. Tsuru, S. Kodaira, P. R. Cummins, and Y. Kaneda (2002), Splay fault branching along the Nankai subduction zone, *Science*, *297*, 1157–1160, doi:10.1126/science.1074111.

Raimbourg, H., Y. Hamano, S. Saito, M. Kinoshita, and A. Kopf (2011), Acoustic and mechanical properties of

Nankai accretionary prism core samples, *Geochem. Geophys. Geosyst.*, *12*, Q0AD10, doi:10.1029/2010GC003169.

Saffer, D., L. McNeill, E. Araki, T. Byrne, N. Eguchi, S. Toczko, K. Takahashi, and the Expedition 319 Scientists (2009), NanTroSEIZE Stage 2: NanTroSEIZE riser/riserless observatory, *Integr. Ocean Drill. Program Prelim. Rep.*, *319*, doi:10.2204/iodp.pr.319.2009.

Seno, T., S. Stein, and A. E. Gripp (1993), A model for the motion of the Philippine Sea plate consistent with NUVEL-1 and geological data, *J. Geophys. Res.*, *98*, 17,941–17,948, doi:10.1029/93JB00782.

Tanioka, Y., and K. Satake (2001), Detailed coseismic slip distribution of the 1944 Tonankai earthquake estimated from tsunami waveforms, *Geophys. Res. Lett.*, *28*, 1075–1078, doi:10.1029/2000GL012284.

Tsuji, T., H. Tokuyama, P. Costa Pisani, and G. Moore (2008), Effective stress and pore pressure in the Nankai accretionary prism off the Muroto Peninsula, southwestern Japan, *J. Geophys. Res.*, *113*, B11401, doi:10.1029/2007JB005002.

Tsuji, T., J.-O. Park, G. Moore, S. Kodaira, Y. Fukao, S. Kuramoto, and N. Bangs (2009), Intraoceanic thrusts in the Nankai Trough off the Kii Peninsula: Implications for intraplate earthquakes, *Geophys. Res. Lett.*, *36*, L06303, doi:10.1029/2008GL036974.

Tsuji, T., J. Dvorkin, G. Mavko, N. Nakata, T. Matsuoka, A. Nakanishi, S. Kodaira, and O. Nishizawa (2011), V_P/V_S ratio and seismic anisotropy in the Nankai Trough seismogenic zone: Insights into effective stress, pore pressure and sediment consolidation, *Geophysics*, *76*, WA71–WA82, doi:10.1190/1.3560018.

Wang, K., and Y. Hu (2006), Accretionary prism in subduction earthquake cycles: The theory of dynamic Coulomb wedge, *J. Geophys. Res.*, *111*, B06410, doi:10.1029/2005JB004094.

Yilmaz, O., and S. Doherty (Eds.) (2001), *Seismic Data Processing*, 2nd ed., Soc. of Explor. Geophys., Tulsa, Okla.

Zimmer, M., M. Prasad, and G. Mavko (2002), Pressure and porosity influences on V_P-V_S ratio in unconsolidated sands, *Lead. Edge*, *21*, 178–183, doi:10.1190/1.1452609.